Nano Research

Open Access

Research Article

In-situ derive hierarchical Ti_3C_2@C@ZnO heterointerface for electromagnetic absorption enhancement

Jianxi Liu[1,2] ✉, Haowen Luo[1], Guohong Wang[1,3], Sirui Han[1], Kai Li[1], Yunyi Zhang[1], Xingmin Liu[4] ✉, Fang Ye[1], and Yadong Xu[2] ✉

[1] *State Key Laboratory of Solidification Processing, Center of Advanced Lubrication and Seal Materials, Northwestern Polytechnical University, Xi'an 710072, China*
[2] *MIIT Key Laboratory of Radiation Detection Materials and Devices, Northwestern Polytechnical University, Xi'an 710072, China*
[3] *Shanxi Semisic Crystal Co., Ltd. Taiyuan 030062, China*
[4] *Dipartimento di Ingegneria Meccanica-Settore Materiali, University of Padova, Padova 35122, Italy*

Cite this article: *Nano Research*, **2025**, *18*, 94907168. https://doi.org/10.26599/NR.2025.94907168

ABSTRACT: Heterointerfaces formed by the intimate connection of different materials with electromagnetic losses are expected to achieve stronger electromagnetic (EM) absorption. However, constructing composites with heterointerfaces still faces great challenges in facile preparation process, optimized impedance matching, high reflection loss (R_L), and ultrathin matching thickness. In this work, we develop ZIF-8 functionalized MXene to produce hierarchical Ti_3C_2@C@ZnO composites with heterointerface to advance EM absorption enhancement. Modified with polydopamine (PDA), few-layer $Ti_3C_2T_x$ MXene sheets enable adsorption of Zn^{2+} metal ions on $Ti_3C_2T_x$@PDA by electrostatic interaction for *in-situ* growth of ZIF-8. Ti_3C_2/C/ZnO heterointerface were obtained after heat treatment of $Ti_3C_2T_x$@PDA@ZIF-8 nanocomposites at various temperatures. The Ti_3C_2/C/ZnO-600 °C with 1.15 mm thickness have a R_L of −50.241 dB and an effective absorption bandwidth of 3.50 GHz. In-depth studies on the electromagnetic loss mechanisms reveal that Ti_3C_2, carbon, and ZnO in nanocomposites generate multiple interfacial polarization losses beyond partial conductivity losses caused by Ti_3C_2 and ZnO. Oxygen vacancy defects in ZnO form dipole losses with carbon. This work not only provides a simple and effective concept for preparing MXene@MOFs heterogeneous composites as an ultrathin and strong electromagnetic wave absorber, but also offers a vital guideline to fabricate various metal oxides derived from the MXene and metal-organic frameworks (MOFs) precursors.

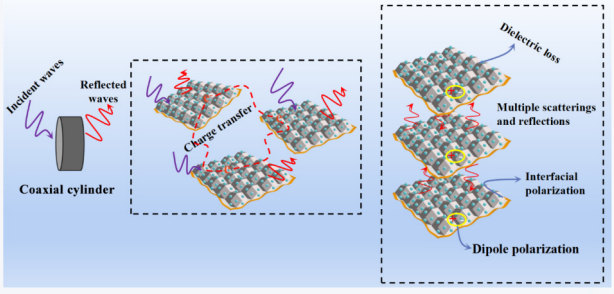

KEYWORDS: MXene, metal-organic frameworks (MOFs)-derived carbon, electromagnetic absorption, heterostructure

1 Introduction

The rapid development of communication technologies, such as wireless communication facilities, electronic terminal equipment and fifth- or sixth-generation (5G/6G) networks, has brought convenience to consumers [1–3]. However, the negative impact of electromagnetic (EM) pollution and radiation from electronic devices during signal reception on human health has garnered widespread attention [4–6]. To address these concerns, EM waves shielding and absorbing materials have been integrated into various electronic devices and appliances [7–9]. Particularly, EM absorption devices effectively protect against EM interference and radiation by converting EM wave energy into thermal energy, thus attenuating the waves [10, 11].

The exploration of comprehensive EM absorption materials with outstanding absorption bandwidth, strong absorption capacity, low density, and minimal thickness have captured the interest of many researchers. Novel carbon materials, including graphite [12, 13], graphene [14, 15], carbon nanotubes [16, 17], carbon fiber [18, 19], and MXenes [20, 21], etc., are being considered as excellent candidates for EM absorption due to their high conductivity and low density. MXenes have been extensively utilized in electrode materials and heat transfer applications related to electronic devices. The accordion-like structure, abundant functional groups, and

Received: November 11, 2024; **Revised:** November 28, 2024
Accepted: December 2, 2024

✉Address correspondence to Jianxi Liu, jianxiliu@nwpu.edu.cn; Xingmin Liu, liuxingmin19890101@126.com; Yadong Xu, xyd220@nwpu.edu.cn

excellent electrical conductivity of MXenes contribute to its EM absorption performance [22, 23]. However, the predominant electrical conductivity, and defect and dipole induced polarization loss mechanism of MXenes negatively impacts EM absorption performance, leading to unsatisfactory reflection losses and narrow absorption bandwidths [24]. Integrating metal oxide particles with MXene by optimizing the impedance matching and construction of nanoscale heterointerface could be a promising and effective method to obtain high-performance EM waves absorption materials. Therefore, the construction of MXenes-based composites with metal oxides, such as Ni/TiO_2/MXene [25], $CoFe_2O_4$/MXene [26], Fe@TiO_2/MXene [27], $NiCo_2O_4$/MXene [28], can effectively improve impedance matching and interface polarization loss at little cost to their EM waves energy attenuation performance.

Metal-organic frameworks (MOFs), composed of metal atoms and organic ligands [29], have attracted significant interest as EM absorption materials [30]. Due to the easily regulated microstructure, MOFs-derived metal/metal oxide-doped porous carbon can be structurally designed at the micro/nano scale, which is advantageous for improving EM absorption performance. Upon pyrolysis at high temperature, zeolite-imidazole framework (ZIF-8), combining Zn^{2+} ions and 2-methylimidazole (2-MIM) [31], can transform into a mixture of ZnO and pyrolytic carbon while retaining the original MOF topology [32]. The combination of $Ti_3C_2T_x$ derived Ti_3C_2 and ZIF-8 derived ZnO and carbon could be a solution for optimizing the impedance matching and construction of nanoscale heterointerface. Hence, ZIF-8 serves as an excellent precursor for regulating the EM absorption performance of MXenes and fabricating highly efficient EM absorbers.

Here, we report the synthesis of Ti_3C_2@C@ZnO nanocomposites for the remarkable EM interference suppression. The study investigates the effects of microstructure and phase composition changes of $Ti_3C_2T_x$@PDA@ZIF-8 derived Ti_3C_2@C@ZnO composites on dielectric and absorbing properties. The excellent absorption performance of $Ti_3C_2T_x$@C@ZnO after mixed carbonization is primarily attributed to the synergy of great impedance matching characteristics, establishment of multiple loss mechanism, optimized conductivity loss, and EM wave absorption mechanisms like multiple scattering.

2 Experimental section

2.1 Materials and chemicals

In this work, all chemicals were of analytical grade and were not further purified. Lithium fluoride (LiF, ≥ 99%), hydrochloric acid solution (HCl, 40 wt.%), and tris-hydrochloride buffer were purchased from Aladdin Biochemical Polytron Technologies, Inc. Ti_3AlC_2 powder (≥ 98% purity) was purchased from China Lianxin Technology, Beijing Ltd. Zinc nitrate hexahydrate ($Zn(NO_3)_2{\cdot}6H_2O$) was purchased from Tianjin Wind Ship Chemical Reagent Technology Co., Ltd. 2-MIM was purchased from Sahn Chemical Technology (Shanghai) Co., Ltd. Dopamine hydrochloride was purchased from Alfa Essa (China) Chemical Co., Ltd. Served as the base material for experimental absorbing agent, paraffin wax was purchased from Sinopharm Chemical Reagent Company.

2.2 Synthesis of few-layer $Ti_3C_2T_x$ MXene sheets

Ti_3AlC_2 powder (2 g) was slowly introduced into HF solution (20 mL, 40%), and stirred at 40 °C to etch the aluminum elements from the MAX phase and peel off the MXene flakes. After 24 h, the suspension was centrifuged at 4000 rpm (5 min) to separate the suspended liquid, and the final pellet was discarded. The suspension obtained underwent a faster centrifugation (10,000 rpm). After that, the obtained MXene sediments were collected, and the resulting precipitate was washed with deionized water until the pH value became 6. Finally, a thin layer of $Ti_3C_2T_x$ powder was obtained through freeze-drying.

2.3 Synthesis of MXene@PDA

The 500 mg of as-prepared monolayer $Ti_3C_2T_x$ was dispersed in 40 mL of tris-hydrochloride buffer, and the pH value of the solution was adjusted to 9. Subsequently, dopamine hydrochloride was added in an amount consistent with the mass of the monolayer $Ti_3C_2T_x$, and the mixture was stirred magnetically for 30 min at 600 rpm in dark environment. At that time, dopamine hydrochloride underwent a polymerization reaction on the surface of MXenes and became polydopamine (PDA). The resulting product was centrifuged at least twice with deionized water at a rate ranging from 5000 to 12,000 rpm (10 min each time).

2.4 Preparation of $Ti_3C_2T_x$@PDA@ZIF-8 composites

The polydopamine-modified $Ti_3C_2T_x$ was dispersed in a 40 mL methanol solution, and $Zn(NO_3)_2{\cdot}6H_2O$ with varying masses (0.15, 0.25, 0.5, and 1.0 g) were added. The mixture was stirred at room temperature for 30 min, allowing Zn^{2+} to adsorb onto the surface of the polydopamine-modified $Ti_3C_2T_x$ precursor through electrostatic interaction. Afterward, the mixture was washed three times with methanol. Meanwhile, an equivalent amount of 2-MIM as that of $Zn(NO_3)_2{\cdot}6H_2O$ was dispersed in 20 mL of methanol solution and sonicated for 20 min to achieve uniform dispersion. Subsequently, the $Ti_3C_2T_x$@PDA@Zn^{2+} mixture was added to this dispersion and stirred at room temperature for 24 h. After that, the resulting mixture was centrifuged and washed three times with methanol solution. Finally, the products were freeze-dried to obtain $Ti_3C_2T_x$@PDA@ZIF-8 composites with different mass ratios. Based on the mass ratio of MXene and $Zn(NO_3)_2{\cdot}6H_2O$, there were named as $Ti_3C_2T_x$@PDA@ZIF-8-0.3 (MXene:$Zn(NO_3)_2{\cdot}6H_2O$ = 0.5 g:0.15 g), $Ti_3C_2T_x$@PDA@ZIF-8-0.5, $Ti_3C_2T_x$@PDA@ZIF-8-1.0, and $Ti_3C_2T_x$@PDA@ZIF-8-2.0.

2.5 Preparation of Ti_3C_2@C@ZnO composites

Regarding the choice of heat treatment temperature: If the annealing temperature is lower than 500 °C, ZIF-8 is not fully converted to ZnO; if the temperature is higher than 700 °C, Zn monomers are produced; if the temperature is further increased to 900 °C, the Zn monomers are vaporized and only carbon remains. The prepared $Ti_3C_2T_x$@PDA@ZIF-8 composites were heated at 550, 600, and 650 °C in a tube furnace with a heating rate of 2 °C/min, and maintained within Ar atmosphere for 2 h. Upon heating, the precursor gradually transformed into the Ti_3C_2@C@ZnO composites with varying structures. Based on the pyrolysis temperature, the MXenes-based nanocomplexes were labeled as Ti_3C_2@C@ZnO-550, Ti_3C_2@C@ZnO-600, and Ti_3C_2@C@ZnO-650.

2.6 Materials characterization

The morphologies and nanostructure of the precursor and obtained nanocomplexes were analyzed by scanning electron microscopy (SEM; ZEISS Sigma 300, 10 kV) and transmission electron

microscopy (TEM; Talos F200X, 200 kV), equipped with energy dispersive X-ray spectroscopy (EDS). Crystallinity and phase purity were tested via X-ray diffraction (XRD; Bruker D8-Advance X) equipped with Cu/Kα radiation (λ = 1.54056 Å) over the 2θ ranging from 5° to 80° with a continuous scan step of 0.02° at 40 kV and 40 mA. X-ray photoelectron spectroscopy (XPS; PHI 5000 VersaProbe III) with Al Kα X-ray radiation under vacuum conditions was utilized for element composition and chemical valence state analysis. The chemical structures were determined using Fourier transform infrared spectrometer (FTIR, Bruker Tensor II). The structure of carbon materials was tested by Raman spectrum (Renishaw inVia Reflex, 514.5 nm). The permittivity of as-prepared Ti_3C_2@C@ZnO composites was tested by an Agilent Technologies E8362B vector network analyzer (VNA) via the waveguide method over the frequency range of 2 to 18 GHz.

3 Results and discussion

3.1 Preparation process

Figure 1 illustrates the detailed fabrication process of the Ti_3C_2@C@ZnO composites. Initially, the two-dimensional (2D) layered MXene nanosheets were synthesized by the typical LiF-HCl etching method. Then, Zn^{2+} ions could be uniformly dispersed on the surface of PDA, because PDA was obtained by polymerization on the MXene surface. Subsequently, by adding 2-MIM, ZIF-8 nanoparticles were facilely synthesized *in situ* on the MXene@PDA. Finally, the samples were heat-treated, and the $Ti_3C_2T_x$, PDA, and ZIF-8 converted to Ti_3C_2, carbon, and ZnO, respectively. Therefore, this transformation process fabricates the novel 2D layered nanocomposites of Ti_3C_2@C@ZnO with heterointerfaces for potential application in EM absorption.

3.2 Crystalline phase and microstructure

The crystal structure and composition of the $Ti_3C_2T_x$, ZIF-8, $Ti_3C_2T_x$@PDA@ZIF-8, and Ti_3C_2@C@ZnO carbonized at 550, 600, and 650 °C were characterized by XRD (Figs. 2(a) and 2(b)). In Fig. 2(a), the typical peaks corresponding to the (002) palne of $Ti_3C_2T_x$ was observed at 7.23°, which revealed that the layer spacing of $Ti_3C_2T_x$ was 1.20 nm [33]. After electrostatic self-assembly, new peaks appeared at 7.2°, 10.25°, 12.6°, and 17.9°, which indicated the successful modification of ZIF-8 on $Ti_3C_2T_x$. $Ti_3C_2T_x$@PDA@ZIF-8 composites with varying ZIF-8 contents were also successfully synthesized by XRD characterization (Fig. S1 in the Electronic Supplementary Material (ESM)). After heat treatment of $Ti_3C_2T_x$ at 600 °C, the peak corresponding to its (002) crystal plane was left-shifted on the XRD spectrum (Fig. S2(a) in the ESM). Also, the increased intensity of 60.8° peak and the presence of characteristic peaks of ZnO at 31.7° and 34.1° indicated that the ZIF-8 has been converted to ZnO and C [34, 35] (Fig. S2(b) in the ESM). The XRD spectrum of the $Ti_3C_2T_x$@PDA@ZIF-8 nanocomposites after heat treatment at different temperatures are shown in Fig. 2(b), in which the characteristic peaks of Ti_3C_2 and ZnO were observed, indicating that there is no obvious change in the phase composition of Ti_3C_2@C@ZnO composites obtained at different temperatures.

To investigate the chemical structure of samples, we conducted the FTIR measurements of $Ti_3C_2T_x$, ZIF-8, $Ti_3C_2T_x$@PDA@ZIF-8, and Ti_3C_2@C@ZnO (Fig. 2(c)). After synthesizing ZIF-8 *in-situ* on the $Ti_3C_2T_x$ surface, stretching vibrations of –OH groups of $Ti_3C_2T_x$ and ZIF-8 were observed at 3400 cm^{-1}. Peaks corresponding to ZIF-8, such as the bending peak of C–H (752 cm^{-1}) and the stretching peak of C–N (995 cm^{-1}), were detected in $Ti_3C_2T_x$@PDA@ZIF-8 nanocomposites. Nucleation of ZIF-8 crystals was promoted by graphitized materials modified with oxygen-containing groups through strong interactions between 2-MIM, Zn^{2+} ions, and other functional groups. The bond stretching vibrations of Ti_3C_2@C@ZnO nanocomposites composed of heat-treated $Ti_3C_2T_x$ and ZIF-8 correspond to each other (Fig. S3 in the ESM).

Figure 2(d) depicts the Raman spectrum of Ti_3C_2@C@ZnO carbonized at 550, 600, and 650 °C, which gives a detailed insight

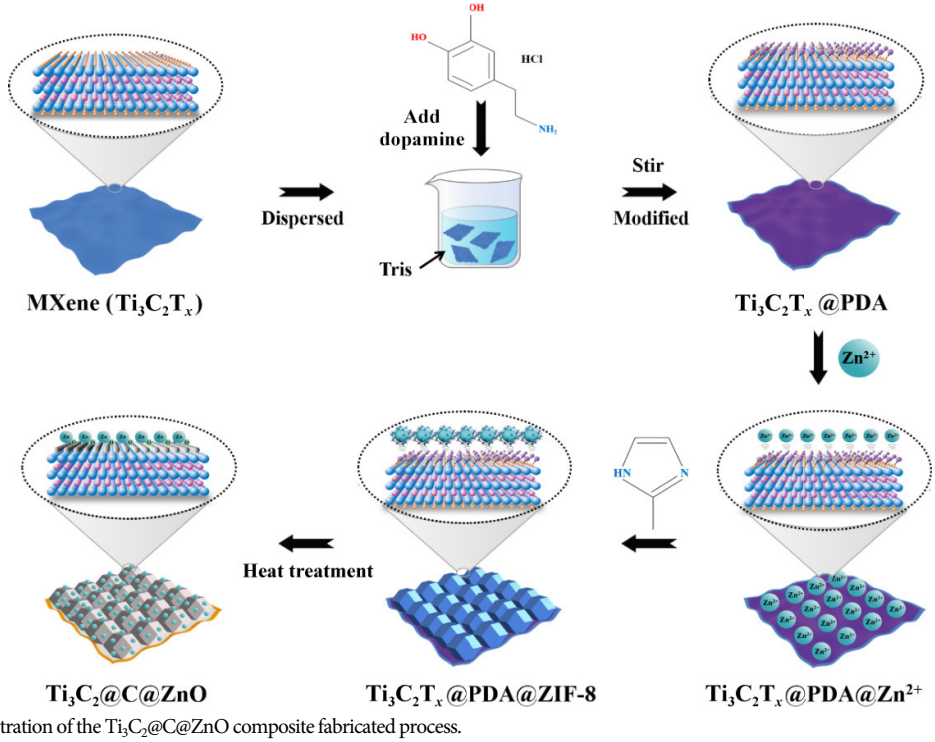

Figure 1 Schematic illustration of the Ti_3C_2@C@ZnO composite fabricated process.

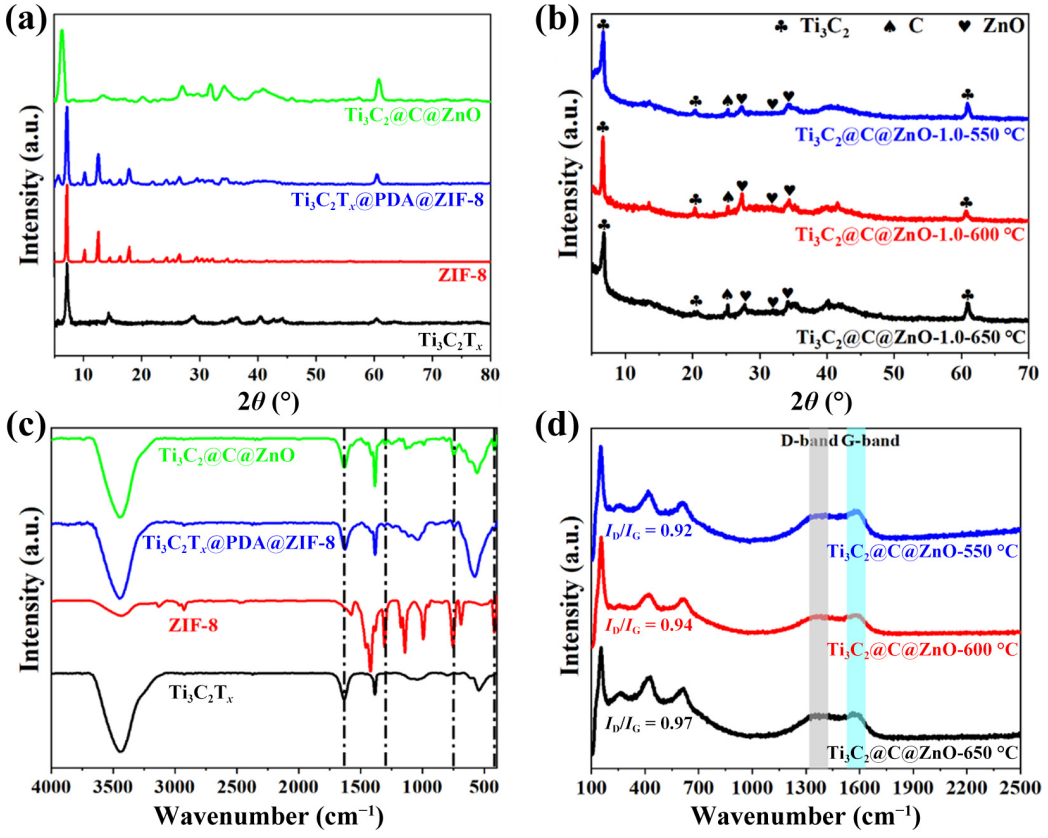

Figure 2 Chemical structure characterization. (a) XRD curves of $Ti_3C_2T_x$, ZIF-8, $Ti_3C_2T_x$@PDA@ZIF-8, and Ti_3C_2@C@ZnO. (b) XRD curves of Ti_3C_2@C@ZnO at different heat treatment temperatures. (c) FTIR spectra of $Ti_3C_2T_x$, ZIF-8, $Ti_3C_2T_x$@PDA@ZIF-8, and Ti_3C_2@C@ZnO. (d) Raman spectra of Ti_3C_2@C@ZnO at different heat treatment temperatures.

into the carbon structure. Four characteristic peaks of Ti_3C_2@C@ZnO appeared at 154, 262, 408, and 605 cm^{-1}, which corresponded to the out-of-plane vibrations of Ti atoms (A_{1g}(Ti, O, C)), vibrations of surface groups (E_g(T_x=O) and E_g(M–T_x)), and vibrations of carbon atoms (A_{1g}(C)), respectively. Besides, the peaks, corresponding to the characteristic D and G bands of carbon, appeared at 1350 and 1580 cm^{-1}, attributed to the defects in the carbon lattice and in-plane stretching vibrations of sp^2 hybridization, respectively. The intensities ratio between D and G (I_D/I_G) of Ti_3C_2@C@ZnO carbonized at 550, 600, and 650 °C were 0.92, 0.94, and 0.97, respectively. Therefore, the increasing I_D/I_G values for 550 to 650 °C indicate that the graphitization intensified as the temperature increased, resulting in more defects and disordered carbon precursors in the Ti_3C_2@C@ZnO composite.

To examine the morphological evolution of $Ti_3C_2T_x$ to Ti_3C_2@C@ZnO composites, the microstructures of all samples were captured via SEM (Fig. 3). At first, the 2D laminated structure of $Ti_3C_2T_x$ is clearly exhibited in Figs. 3(a) and 3(a1), indicating that the MAX phase was effective stripped by HF. After the polymerization reaction on the $Ti_3C_2T_x$ surface to cover the PDA, $Ti_3C_2T_x$@PDA appeared to be smoother compared to the pristine $Ti_3C_2T_x$ (Figs. 3(b) and 3(b1)). Upon Zn^{2+} adsorption, ortho-octahedral ZIF-8 was synthesized *in-situ* on the $Ti_3C_2T_x$@PDA surface in a homogeneous dispersion with only tens nanometers particle size, which enhanced the microstructure of the complex interface (Figs. 3(c) and 3(c1)). During heat treatment, the Zn element in ZIF-8 was converted directly to ZnO by calcination at 550 °C, but metallic Zn was also present in the temperature range from 800 to 908 °C, even evaporating at temperature close to 908 °C [36, 37]. Consistent with the Zn evaluation rule described above, the size of the ZnO particles formed by ZIF-8 carbonation on the Ti_3C_2@C@ZnO surface decreased as the heat treatment temperature was increased from 550 to 650 °C (Figs. 3(d)–3(f)).

To investigate the evolution of the chemical properties in $Ti_3C_2T_x$@PDA@ZIF-8 and its derivative Ti_3C_2@C@ZnO composites, XPS with binding energies ranging from 0 to 800 eV was employed to analyze the elements and components in the samples (Fig. 4). Figures S4(a) and S4(b) in the ESM show the C 1s and Ti 2s fine spectrums of $Ti_3C_2T_x$ with fitting peaks: Six distinct peaks in the C 1s fine spectrum were C–F, C–O, C–C, C=C, C–Ti–O, and C–Ti; five distinct peaks in the Ti 2s fine spectrum were Ti(II) $2p_{1/2}$, Ti–C $2p_{1/2}$, Ti–O, Ti(II) $2p_{3/2}$, and Ti–C $2p_{3/2}$. However, after heat treatment of $Ti_3C_2T_x$ at 600 °C, the peak strength of C–Ti was significantly weakened, mainly due to severe oxidation (Figs. S4(c) and S4(d) in the ESM). In the XPS spectrum of $Ti_3C_2T_x$@PDA@ZIF-8 (Fig. S5(a) in the ESM), the C–N bond (385.2 eV) was observed in the C 1s with an increase in the intensity of the C=C bond, which was mainly attributed to the formation of ZIF-8. In the XPS spectrum of Ti_3C_2@C@ZnO-600 °C, the peak belonging to Zn $2p_{1/2}$ and Zn $2p_{3/2}$ were located at 1021.4 and 1045.0 eV, respectively (Fig. S5(b) in the ESM). Furthermore, due to the severe oxidation of $Ti_3C_2T_x$ and decomposition of ZIF-8, the C–N, C=C and some reactive bonds (e.g., C–O) of the $Ti_3C_2T_x$@PDA@ZIF-8 nanocomposites were weakened, as evidenced by the XPS spectrum of Ti_3C_2@C@ZnO-600 °C (Fig. S5(b) in the ESM), C 1s (Fig. 4(d)), Ti 2p (Fig. 4(e)), and Zn 2p (Fig. 4(f)).

Typical layered $Ti_3C_2T_x$ with a monolayer structure within

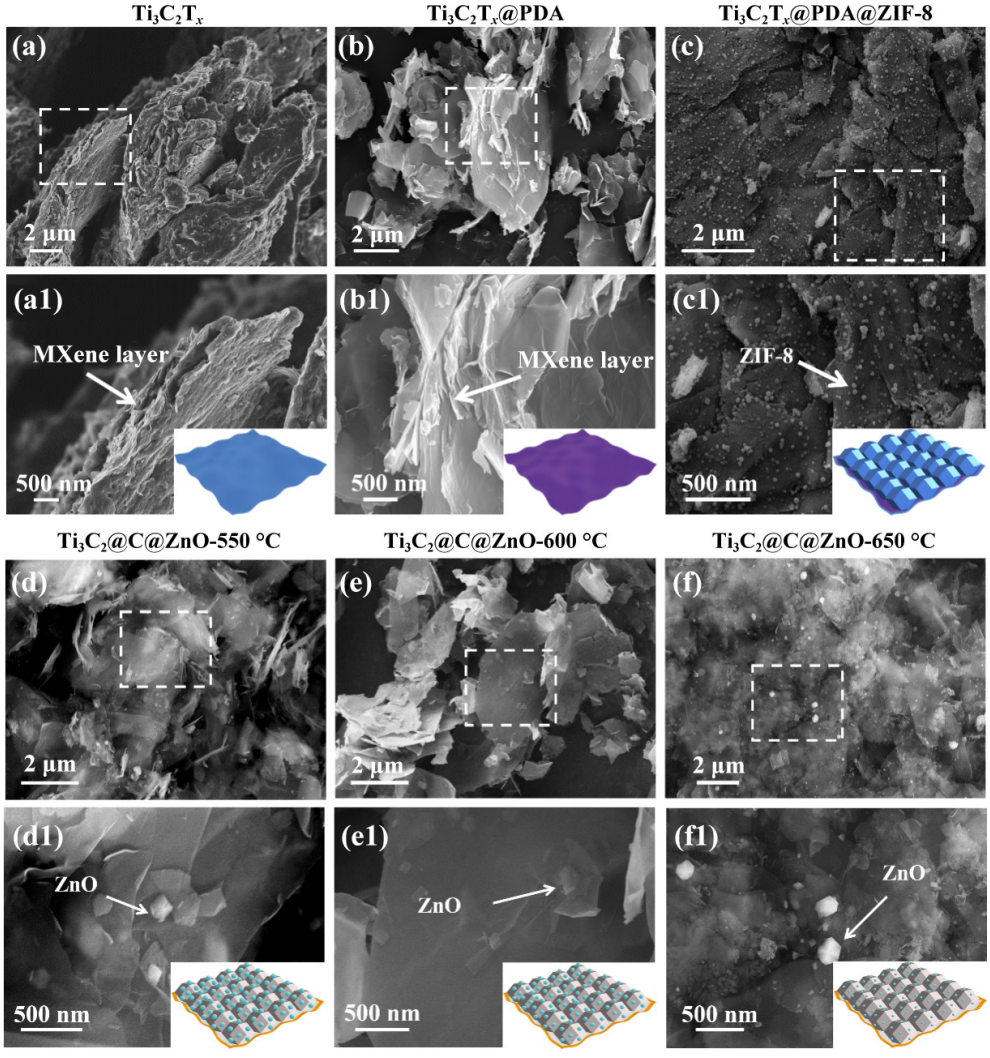

Figure 3 SEM microstructure characterization. The SEM images of (a) and (a1) MXene, (b) and (b1) $Ti_3C_2T_x$ @PDA, (c) and (c1) $Ti_3C_2T_x$@PDA@ZIF-8, (d) and (d1) Ti_3C_2@C@ZnO-550 °C, (e) and (e1) Ti_3C_2@C@ZnO-600 °C, (f) and (f1) Ti_3C_2@C@ZnO-650 °C.

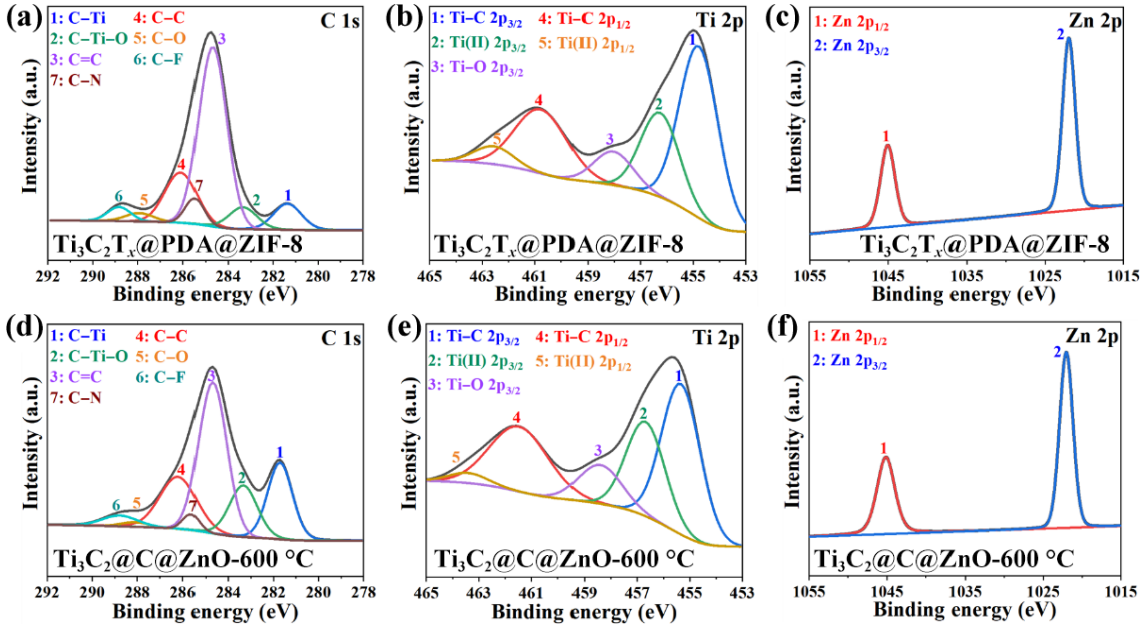

Figure 4 Chemical composition of $Ti_3C_2T_x$@PDA@ZIF-8 and Ti_3C_2@C@ZnO. The XPS survey of $Ti_3C_2T_x$@PDA@ZIF-8, with peak fitting results in (a) C 1s, (b) Ti 2p, and (c) Zn 2p regions. The XPS survey of Ti_3C_2@C@ZnO-600 °C, with peak fitting results in (d) C 1s, (e) Ti 2p, and (f) Zn 2p regions.

$Ti_3C_2T_x$@PDA@ZIF-8 was clearly observed in Figs. 5(a) and 5(b), which is consistent with the morphology in SEM images. Besides, ortho-octahedral ZIF-8 were observed on the $Ti_3C_2T_x$ surface (Fig. 5(b) and Fig. S6 in the ESM), indicating that the adsorption of Zn^{2+} on $Ti_3C_2T_x$ was enhanced after PDA treatment. For analyzing the crystal structure of $Ti_3C_2T_x$@PDA@ZIF-8, the selected area electron diffraction (SAED) pattern (Fig. 5(c)) was in good agreement with a previous study [38], which exhibited diffraction rings related to $Ti_3C_2T_x$ (002) and ZIF-8 (110) and (200) [37, 39]. Moreover, Figs. 5(d)–5(f) depict TEM images of Ti_3C_2@C@ZnO-600 °C after heat treatment of $Ti_3C_2T_x$@PDA@ZIF-8 at 600 °C. Specifically, the lamellar structure of $Ti_3C_2T_x$ was preserved, indicating its good high-temperature stability. Although some surface functional groups (–OH, –F, etc.) disappeared with increasing temperature, the layered structure remains unchanged below 1000 °C [40]. Also, the ortho-octahedral ZIF-8 was retained after heat treatment at 600 °C, indicating that the microstructure of ZIF-8 was preserved even after $Ti_3C_2T_x$@PDA@ZIF-8 was transformed from the organic to the inorganic state. However, the PDA on the $Ti_3C_2T_x$ surface was converted to pyrolytic carbon at high temperature and served as an additional carbon source to supplement the pyrolytic carbon generated by the ZIF-8 pyrolysis process. Notably, the ortho-dodecahedral ZnO decreased in size and transitioned from a dense to a loose structure, which is consistent with the SEM images. The formation pyrolytic carbon and ZnO could lead to the formation of $Ti_3C_2T_x$/C and C/ZnO hetero nanointeface, which will contribute interface polarization loss. Moreover, the formation of hierarchical structure will improve the impedance matching of $Ti_3C_2T_x$. The lattice distance of 0.28 nm matched the crystal plane of ZnO (100) obtained from ZIF-8 pyrolysis (Fig. 5(f)). Furthermore, Fig. 5(g) displays the EDS mappings obtained on Ti_3C_2@C@ZnO-600 °C, highlighting the presence of C, O, Zn, and Ti elements. The homogeneous distribution of these elements on the Ti_3C_2@C@ZnO surface ensures great interfacial polarization, which enhances the capacity of EMA [41].

3.3 EM properties

The complex permittivity of all samples was tested using a vector network analyzer based on the waveguide method after mixing with paraffin wax (50 wt.% paraffin content). Because the pyrolysis

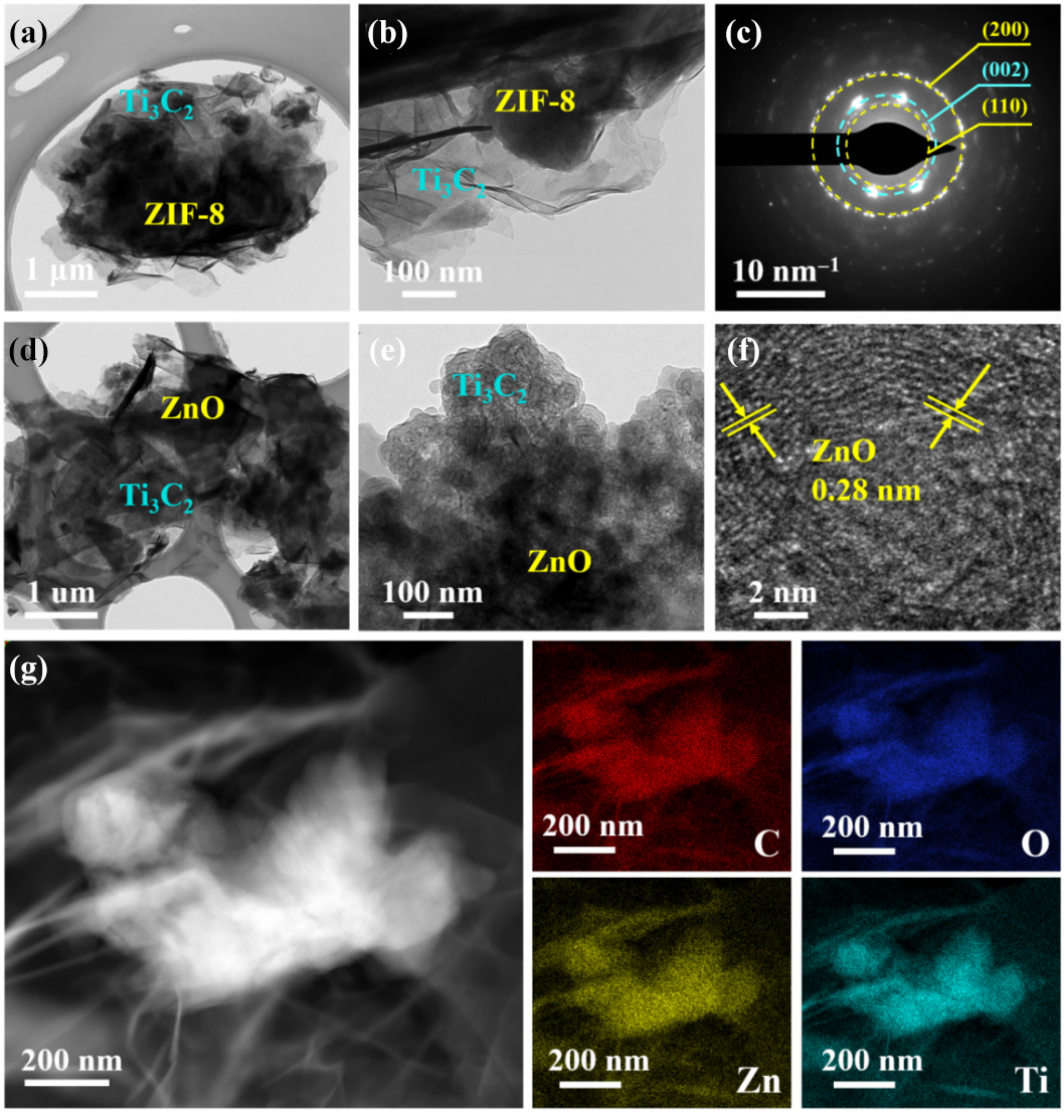

Figure 5 TEM microstructure characterization. The TEM images of (a)–(c) $Ti_3C_2T_x$@PDA@ZIF-8 and (d)–(f) Ti_3C_2@C@ZnO-600 °C. (g) The EDS mappings of Ti_3C_2@C@ZnO-600 °C.

complexes (C, N, O, and Zn) are not magnetic, the EM absorption is primarily affected by the relative complex permittivity (ε_r) consisting of real (ε') and imaginary (ε'') parts [42, 43]. The ε', ε'' and tanδ ($\varepsilon'/\varepsilon''$) of Ti_3C_2@C@ZnO nanocomposites derived at different temperatures were tested at the frequency ranging from 2 to 18 GHz.

The ε' and ε'' of the Ti_3C_2@C@ZnO nanocomposites with different mass ratio of MXene and ZIF-8 were tested after the heat treatment at 600 °C (Fig. S7 in the ESM). Specifically, with the increase of ZIF-8 addition, the ε' first increased, then decreased, and finally increased again, while the ε'' first increased and then decreased. For pristine $Ti_3C_2T_x$, the ε' and ε'' were 20.04 and 6.79, respectively. For heat-treated Ti_3C_2@C@ZnO, the ε' (ε'') of Ti_3C_2@C@ZnO-0.3, Ti_3C_2@C@ZnO-0.5, Ti_3C_2@C@ZnO-1.0, and Ti_3C_2@C@ZnO-2.0 were 28.08 (11.65), 34.37 (14.14), 20.48 (7.05), and 28.27 (3.28), respectively. The above results illustrate that the capacities of the Ti_3C_2@C@ZnO nanocomposites to absorb and lose EM waves energy are significantly improved, attributed to the formation of more heterointerface and vacancy defects inside the Ti_3C_2@C@ZnO. In particular, the heterointerface formed between Ti_3C_2 and ZnO enhances the polarization effect in the alternating EM field, which leads to an increase in the ε'. Also, the increase in ZnO content improves the electrical conductivity and thus enhances the ε''.

After heat treatment at different temperatures, the ε' and ε'' of Ti_3C_2@C@ZnO-1.0 nanocomposites were tested and shown in Figs. 6(a) and 6(b), demonstrating that the ε' (ε'') of the Ti_3C_2@C@ZnO-550 °C, Ti_3C_2@C@ZnO-600 °C, and Ti_3C_2@C@ZnO-650 °C were 29.87 (8.60), 20.48 (7.05) and 38.30 (6.09), respectively. According to the SEM images, the particle size of ZnO decreased with the increase of the heat treatment temperature, therefore decreasing the electrical conductivity of the nanocomposites, which led to the decrease of the ε''. In addition, Fig. 6(c) shows the dielectric loss (tanδ) of Ti_3C_2@C@ZnO-1.0 nanocomposites after heat treatment at different temperatures. The larger value of tanδ represents the stronger dielectric loss capability of the nanocomposites. Hence, the Ti_3C_2@C@ZnO-600 °C nanocomposite exhibited the strongest EM waves energy loss ability.

Based on the Debye relaxation theory [43], changes in the real and imaginary values of the ε_r usually form a semicircle, i.e., the Cole-Cole semicircle. Each semicircle represents the presence of a Debye relaxation mechanism in the material [44]. Figure 6(d) shows the Cole–Cole semicircles of Ti_3C_2@C@ZnO-550 °C, Ti_3C_2@C@ZnO-600 °C, and Ti_3C_2@C@ZnO-650 °C nanocomposites. All the samples have distinct semicircles, indicating that the microwaves were effectively attenuated and dissipated, which further proofs the existence of various polarization methods and relaxation mechanisms in Ti_3C_2@C@ZnO after heat treatment at different temperatures, improving the EM waves loss capacity.

In Fig. 7, the EM absorption performance of nanocomposites was analyzed based on transmission line theory, which is measured by the reflection loss (R_L) value below −10 dB. Specifically, Ti_3C_2 had the optimal R_L value of 38.679 dB at a thickness of 2.00 mm with an effective absorption bandwidth of 2.00 GHz (Figs. 7(a1)–7(a3)). $Ti_3C_2T_x$@C@ZnO-0.3 had the optimal R_L value of 33.827 GHz at a thickness of 5.40 mm, and an effective absorption bandwidth of 2.40 GHz at a thinner thickness of 0.90 mm, indicating stronger EMA performance (Figs. 7(b1)–7(b3)). The best R_L value of Ti_3C_2@C@ZnO-0.5 was 17.735 dB at 5.05 mm thickness

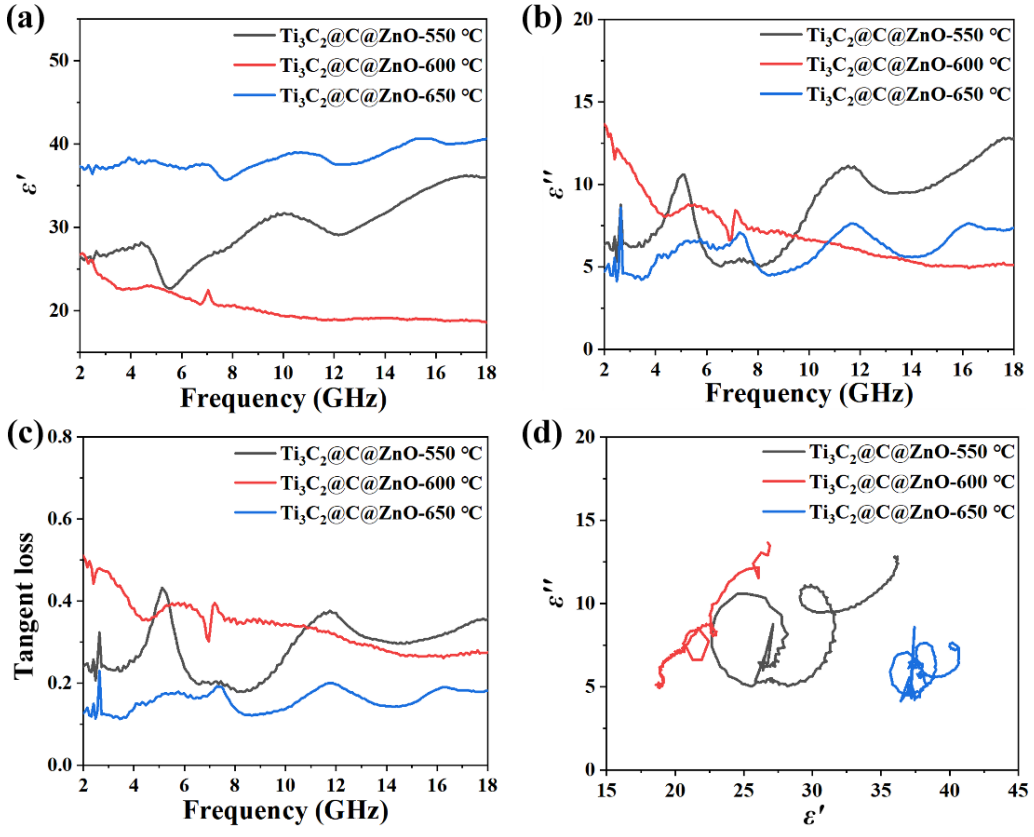

Figure 6 EM absorption and loss mechanism. Frequency dependence of the (a) ε', (b) ε'', (c) tanδ, and (d) the variation of ε' and ε'' with respect to each other of Ti_3C_2@C@ZnO after heat treatment at different temperatures.

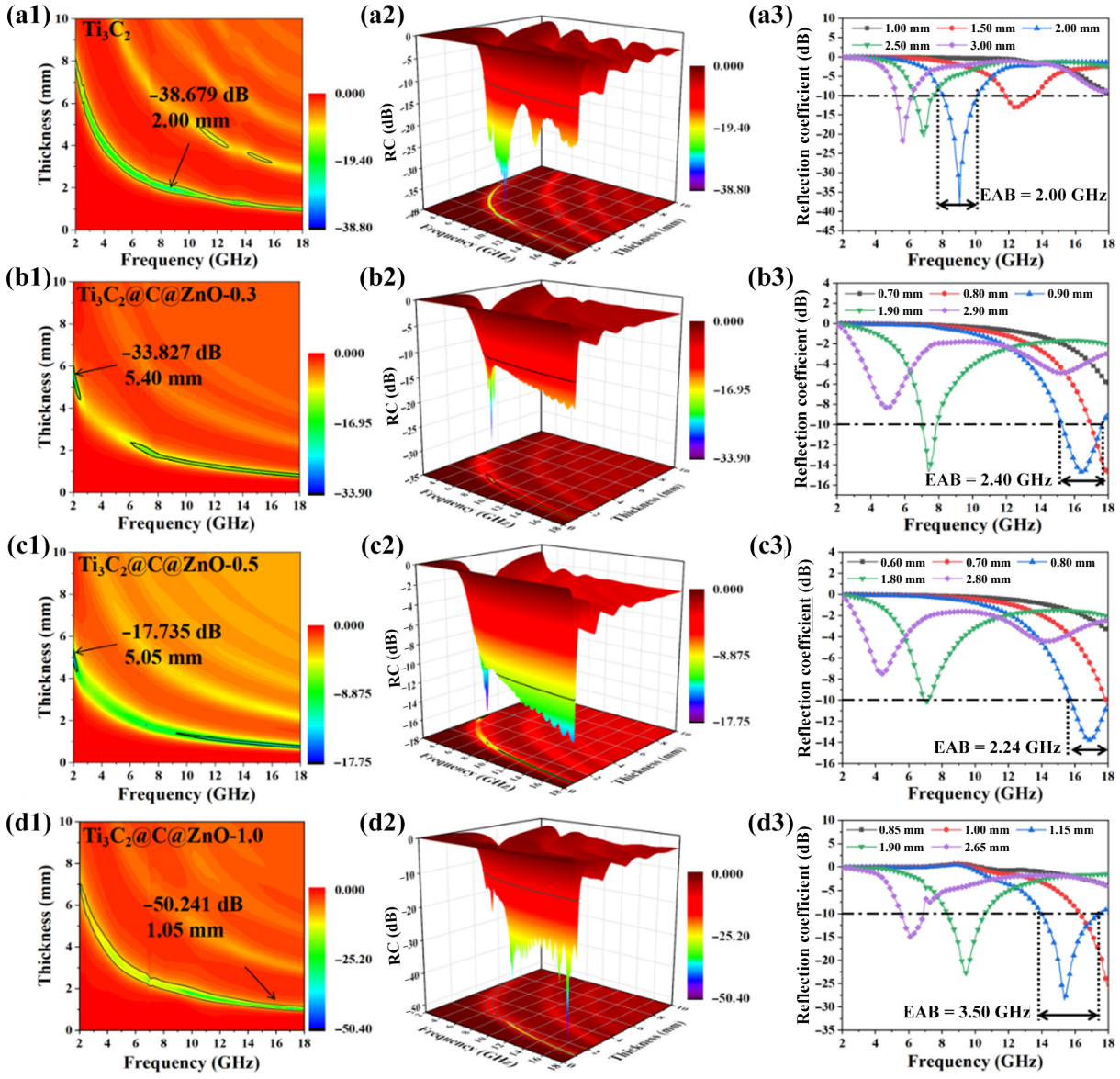

Figure 7 The influence of heterostructure adjustment on EM absorption performance. (a1)–(d1) 2D R_L contour map, (a2)–(d2) 3D and contour plots of the R_C, and (a3)–(d3) the R_C value of Ti_3C_2, Ti_3C_2@C@ZnO-0.3, Ti_3C_2@C@ZnO-0.5, and Ti_3C_2@C@ZnO-1.0 composites versus the frequency and thickness.

and 2.24 GHz effective absorption bandwidth at 0.80 mm thickness (Figs. 7(c1)–7(c3)), which was the thinnest sample. The prime sample was Ti_3C_2@C@ZnO-1.0 (Figs. 7(d1)–7(d3)) with 50.241 dB and 3.50 GHz effective absorption bandwidth at 1.15 mm thickness. Moreover, increasing ZnO content would decrease the EM absorption performance. Specifically, the Ti_3C_2@C@ZnO-2.0 nanocomposites had the narrowest effective absorption bandwidth (only 1.20 GHz) due to an excess of $Ti_3C_2T_x$, which led to a mismatch in material impedance (Fig. S8 in the ESM). After heat treatment at 550 and 650 °C, the reflection coefficient (R_C) curves of Ti_3C_2@C@ZnO nanocomposites were shown with corresponding 2D and 3D images in Fig. S9 in the ESM. The R_C peak bule shifted as the thickness increased, resulting in a decrease effective absorption bandwidth.

The above results of the EM absorption performance underscore that the Ti_3C_2@C@ZnO-1.0 (600 °C) nanocomposite own the best EM absorption performance and effective absorption bandwidth. Despite Ti_3C_2@C@ZnO-0.3 owning high EM waves loss capacity, the excessive dielectric constant largely increases the reflectivity of EM waves on the surface and impedes the entrance into the sample interior, aggravating the EM absorption performance. In short, achieving a balance between impedance matching characteristics and EM waves loss capacity is crucial for ensuring sufficient EM waves entering the absorbent and achieving excellent EM absorption performance.

3.4 Electromagnetic loss mechanisms

The excellent electrical conductivity of $Ti_3C_2T_x$ leads to considerable reflections when used to absorb incident EM waves, since the predominant loss mechanism of $Ti_3C_2T_x$ is electrical conductivity, which prevent the realization of the impedance matching principle [45]. *In situ* growth of ZIF-8 on the $Ti_3C_2T_x$ surface followed by high-temperature heat treatment to decompose ZIF-8 into ZnO and graphite carbon is a strategy to solve the above issue. The obtained Ti_3C_2@C@ZnO can optimize the dielectric constant of the nanocomposites and thus improve the absorption performance.

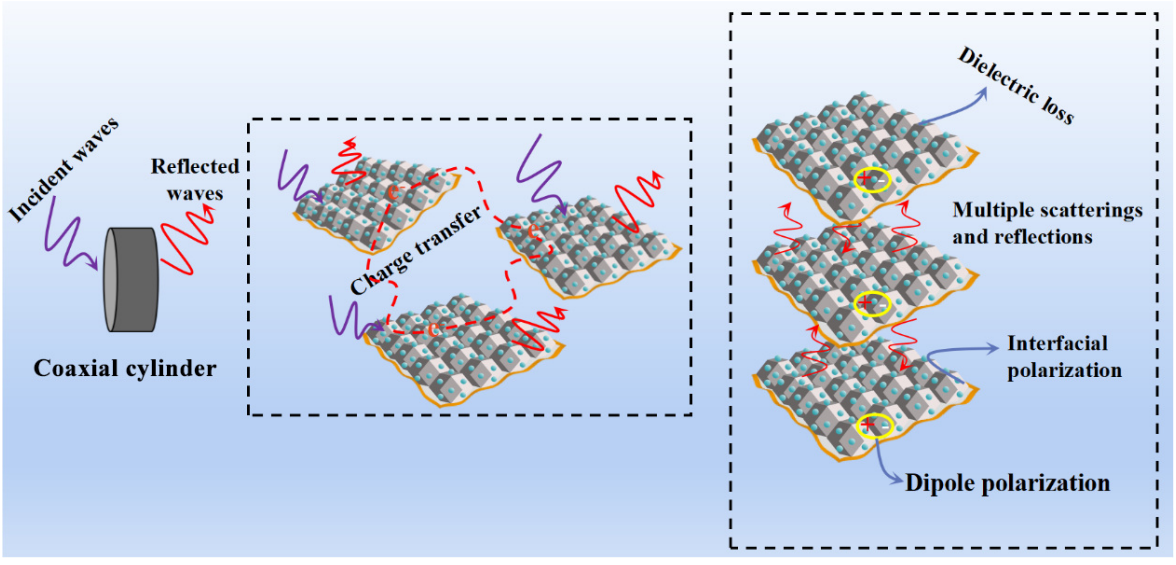

Figure 8 Schematic illustration of EM absorption mechanisms for Ti_3C_2@C@ZnO nanocomposites.

Figure 8 illustrates the interaction mechanism between Ti_3C_2@C@ZnO absorbents and EM waves in an alternating EM field. Firstly, the abundant lamellar structure and semiconducting ZnO in Ti_3C_2@C@ZnO improve the impedance matching characteristics, which reduces the EM waves reflection from the absorbent surface. As a result, EM waves are able to enter the interior of the absorbent, which is crucial for subsequent EM waves loss [46]. Secondly, the layered structure provides additional transmission paths for EM waves, increasing the probability of wave scattering and facilitating energy consumption [47]. Thirdly, the Ti_3C_2@C@ZnO absorbers establish multiple loss mechanisms based on its materials, heterointerfaces, elements, etc. As a semiconductor with low electrical conductivity, ZnO has a limited impact on the conductivity loss. Fortunately, the heterointerface between Ti_3C_2 and carbon, as well as carbon and ZnO improves the polarization loss capability of absorber and promotes impedance matching to extend the propagation path of EM waves. Additionally, vacancy defects and heterointerfaces in the absorbents contribute to the generation of interfacial scattering, spatial charge polarization, and enhanced dielectric relaxation, thereby improving EM waves attenuation. Moreover, the interfaces between Ti_3C_2 and ZnO, Ti_3C_2 and cracked carbon, and ZnO and cracked carbon also affect depolarization, whereas Ti_3C_2@C@ZnO may lead to charge buildup and current path interruption, which further improves EM absorption performance.

4 Conclusions

In summary, 2D layered Ti_3C_2@C@ZnO nanocomposites with tunable EM absorption performance have been synthesized from the $Ti_3C_2T_x$@PDA@ZIF-8 precursors by the *in-situ* growth of ZIF-8 via electrostatic interaction followed by the heat treatment at different temperatures for carbonization. The obtained Ti_3C_2@C@ZnO absorber for EM absorption is a bonded nanocomposite of cleaved carbon and semiconductor ZnO with 2D Ti_3C_2 nanosheets. In this absorber, Ti_3C_2 and ZnO cause some conductive loss due to their intrinsic conductivity, while oxygen vacancy defects in ZnO combine with dipole polarization in carbon to form multiple interface polarization losses. The Ti_3C_2@C@ZnO absorber has an effective absorption bandwidth of 3.50 GHz (from 13.9 to 17.4 GHz) with an optimal R_L of 50.241 dB at an extremely thin thickness of only 1.15 mm. This work develops a great Ti_3C_2@C@ZnO absorber with multiple loss mechanisms for EM absorption, which not only effectively enhances the single loss mechanism of $Ti_3C_2T_x$ and improves the impedance matching, but also offers a vital strategy to fabricate nanocomposites derived from the MXenes@MOFs precursors.

Electronic Supplementary Material: Supplementary material (details of the characterization of $Ti_3C_2T_x$, ZIF-8, $Ti_3C_2T_x$@PDA@ZIF-8, and Ti_3C_2@C@ZnO series (including XRD, FTIR, XPS, TEM), and the EM performance of Ti_3C_2@C@ZnO composites (including ε', ε'', and EM absorption)) is available in the online version of this article at https://doi.org/10.26599/NR.2025.94907168.

Data availability

All data needed to support the conclusions in the paper are presented in the manuscript and the Electronic Supplementary Material. Additional data related to this paper may be requested from the corresponding author upon request.

Acknowledgements

The authors thank the financial support from the National Natural Science Foundation of China (No. 52071270), the National Key Research and Development Program of China (No. 2023YFE0206300), the Natural Science Foundation of Shaanxi Province (No. 2024RS-CXTD-62), the Science Fund of Shandong Laboratory of Advanced Materials and Green Manufacturing (Yantai) (No. AMGM2023F03), and the Research Fund of the State Key Laboratory of Solidification Processing (NPU) (No. 2022-QZ-04). We would like to thank the Analytical & Testing Center of Northwestern Polytechnical University and Shaanxi Materials Analysis and Research Center.

Declaration of competing interest

All the contributing authors report no conflict of interests in this work.

Author contributions

J. X. L.: Project administrration, funding acquisition, writing manuscipt, revising manuscript, reviewing manuscript. H. W. L.: Data curation, validation, writing manuscipt, revising manuscript. G. H. W.: Data curation, validation, writing manuscript, experimental design. S. R. H.: Reviewing manuscript, validation. K. L.: Reviewing manucript. Y. Y. Z.: Reviewing manuscript. X. M. L.: Project administration, reviewing manuscript. F. Y.: Project administration, reviewing manuscript. Y. D. X.: Funding acquisition, project administration.

Use of AI statement

None.

References

[1] Watts, C. M.; Liu, X. L.; Padilla, W. J. Metamaterial electromagnetic wave absorbers. *Adv. Mater.* **2012**, *24*, OP98–OP120.

[2] Chen, Z. P.; Xu, C.; Ma, C. Q.; Ren, W. C.; Cheng, H. M. Lightweight and flexible graphene foam composites for high-performance electromagnetic interference shielding. *Adv. Mater.* **2013**, *25*, 1296–1300.

[3] Yin, X. W.; Kong, L.; Zhang, L. T.; Cheng, L. F.; Travitzky, N.; Greil, P. Electromagnetic properties of Si–C–N based ceramics and composites. *Int. Mater. Rev.* **2014**, *59*, 326–355.

[4] Wei, Q. W.; Pei, S. F.; Qian, X. T.; Liu, H. P.; Liu, Z. B.; Zhang, W. M.; Zhou, T. Y.; Zhang, Z. C.; Zhang, X. F.; Cheng, H. M. et al. Superhigh electromagnetic interference shielding of ultrathin aligned pristine graphene nanosheets film. *Adv. Mater.* **2020**, *32*, 1907411.

[5] Lou, Z. C.; Wang, Q. Y.; Kara, U. I.; Mamtani, R. S.; Zhou, X. D.; Bian, H. Y.; Yang, Z. H.; Li, Y. J.; Lv, H. L.; Adera, S. et al. Biomass-derived carbon heterostructures enable environmentally adaptive wideband electromagnetic wave absorbers. *Nano-Micro Lett.* **2022**, *14*, 11.

[6] Li, M. H.; Lu, X. K.; Zhu, W. J.; Xu, H. L.; Xue, J. M.; Ye, F.; Liu, Y. S.; Fan, X. M.; Cheng, L. F. A sheath–core shaped ZrO_2–SiC/SiO_2 fiber felt with continuously distributed SiC for broad-band electromagnetic absorption. *Chem. Eng. J.* **2021**, *419*, 129414.

[7] Song, P.; Liu, B.; Liang, C. B.; Ruan, K. P.; Qiu, H.; Ma, Z. L.; Guo, Y. Q.; Gu, J. W. Lightweight, flexible cellulose-derived carbon aerogel@reduced graphene oxide/PDMS composites with outstanding EMI shielding performances and excellent thermal conductivities. *Nano-Micro Lett.* **2021**, *13*, 91.

[8] Lu, X. K.; Li, M. H.; Xue, J. M.; Ye, F.; Fan, X. M.; Liu, Y. S.; Cheng, L. F.; Zhang, L. T. A SiC nanowires/$Ba_{0.75}Sr_{0.25}Al_2Si_2O_8$ ceramic heterojunction for stable electromagnetic absorption under variable-temperature. *J. Mater. Sci. Technol.* **2022**, *125*, 29–37.

[9] Lu, X. K.; Li, X.; Zhu, W. J.; Xu, H. L. Construction of embedded heterostructures in biomass-derived carbon frameworks for enhancing electromagnetic wave absorption. *Carbon* **2022**, *191*, 600–609.

[10] Lu, X. K.; Zhu, D. M.; Li, X.; Wang, Y. J. Architectural design and interfacial engineering of CNTs@$ZnIn_2S_4$ heterostructure/cellulose aerogel for efficient electromagnetic wave absorption. *Carbon* **2022**, *197*, 209–217.

[11] Li, X.; Wang, G. H.; Li, Q.; Wang, Y. J.; Lu, X. K. Dual optimized $Ti_3C_2T_x$ MXene@$ZnIn_2S_4$ heterostructure based on interface and vacancy engineering for improving electromagnetic absorption. *Chem. Eng. J.* **2023**, *453*, 139488.

[12] Zhang, Y.; Huang, Y.; Zhang, T. F.; Chang, H. C.; Xiao, P. S.; Chen, H. H.; Huang, Z. Y.; Chen, Y. S. Broadband and tunable high-performance microwave absorption of an ultralight and highly compressible graphene foam. *Adv. Mater.* **2015**, *27*, 2049–2053.

[13] Gao, X. M.; Fu, Y. L.; Jiang, D.; Wang, D. S.; Weng, L. J.; Yang, J.; Sun, J. Y.; Hu, M. Responses of TMDs-metals composite films to atomic oxygen exposure. *J. Alloys Compd.* **2018**, *765*, 854–861.

[14] Liang, J. J.; Wang, Y.; Huang, Y.; Ma, Y. F.; Liu, Z. F.; Cai, J. M.; Zhang, C. D.; Gao, H. J.; Chen, Y. S. Electromagnetic interference shielding of graphene/epoxy composites. *Carbon* **2009**, *47*, 922–925.

[15] Singh, A. P.; Mishra, M.; Chandra, A.; Dhawan, S. K. Graphene oxide/ferrofluid/cement composites for electromagnetic interference shielding application. *Nanotechnology* **2011**, *22*, 465701.

[16] Pan, H. X.; Yin, X. W.; Xue, J. M.; Cheng, L. F.; Zhang, L. T. Microstructures and EMI shielding properties of composite ceramics reinforced with carbon nanowires and nanowires-nanotubes hybrid. *Ceram. Int.* **2017**, *43*, 12221–12231.

[17] Weng, G. M.; Li, J. Y.; Alhabeb, M.; Karpovich, C.; Wang, H.; Lipton, J.; Maleski, K.; Kong, J.; Shaulsky, E.; Elimelech, M. et al. Layer-by-layer assembly of cross-functional semi-transparent MXene-carbon nanotubes composite films for next-generation electromagnetic interference shielding. *Adv. Funct. Mater.* **2018**, *28*, 1803360.

[18] Qiao, J.; Zhang, X.; Xu, D. M.; Kong, L. X.; Lv, L. F.; Yang, F.; Wang, F. L.; Liu, W.; Liu, J. R. Design and synthesis of TiO_2/Co/carbon nanofibers with tunable and efficient electromagnetic absorption. *Chem. Eng. J.* **2020**, *380*, 122591.

[19] Liang, H. S.; Xing, H.; Qin, M.; Wu, H. J. Bamboo-like short carbon fibers@Fe_3O_4@phenolic resin and honeycomb-like short carbon fibers@Fe_3O_4@FeO composites as high-performance electromagnetic wave absorbing materials. *Compos. Part A: Appl. Sci. Manuf.* **2020**, *135*, 105959.

[20] Shahzad, F.; Alhabeb, M.; Hatter, C. B.; Anasori, B.; Hong, S. M.; Koo, C. M.; Gogotsi, Y. Electromagnetic interference shielding with 2D transition metal carbides (MXenes). *Science* **2016**, *353*, 1137–1140.

[21] G.; Shao, Y. W.; Wang, Z.; Jiang, L. T.; Mou, B.; Tian, N.; You, C. Y.; Li, Y. Mechanically robust and multifunctional $Ti_3C_2T_x$ MXene composite aerogel for broadband EMI shielding. *Carbon* **2024**, *221*, 118948.

[22] Han, M. K.; Yin, X. W.; Hantanasirisakul, K.; Li, X. L.; Iqbal, A.; Hatter, C. B.; Anasori, B.; Koo, C. M.; Torita, T.; Soda, Y. et al. Anisotropic MXene aerogels with a mechanically tunable ratio of electromagnetic wave reflection to absorption. *Adv. Opt. Mater.* **2019**, *7*, 1900267.

[23] Wang, G. H.; Liu, J. X.; Liu, X. C.; Li, M. H.; Liu, J. J.; Chai, N.; Ye, F.; Xue, J. M.; Fan, X. M.; Xu, H. L. et al. Oxidation-resistant vitamin C/MXene foam via surface hydrogen bonding for stable electromagnetic interference shielding in air ambient. *Appl. Surf. Sci.* **2023**, *610*, 155396.

[24] Wang, G. H.; Li, M. H.; Liu, J. X.; Ye, F.; Cheng, L. F.; Fan, X. M.; Liu, X. M.; Riedel, R. Robust $Ti_3C_2T_x$ MXene foam modified with natural antioxidants for long-term effective electromagnetic interference shielding. *iScience* **2023**, *26*, 107176.

[25] Zhou, C. L.; Wang, X. X.; Luo, H.; Deng, L. W.; Wei, S.; Zheng, Y. W.; Jia, Q.; Liu, J. Q. Rapid and direct growth of bipyramid TiO_2 from $Ti_3C_2T_x$ MXene to prepare Ni/TiO_2/C heterogeneous composites for high-performance microwave absorption. *Chem. Eng. J.* **2020**, *383*, 123095.

[26] Swapnalin, J.; Koneru, B.; Banerjee, P.; Natarajan, S.; Franco, A. Multilayer intercalation: MXene/cobalt ferrite electromagnetic wave absorbing two-dimensional materials. *J. Phys. Chem. Solids* **2022**, *168*, 110797.

[27] Deng, B. W.; Xiang, Z.; Xiong, J.; Liu, Z. C.; Yu, L. Z.; Lu, W. Sandwich-like Fe&TiO_2@C nanocomposites derived from MXene/Fe-MOFs hybrids for electromagnetic absorption. *Nano-Micro Lett.* **2020**, *12*, 55.

[28] J.; Zhao, C.; Yin, Y. C.; Nie, T. L.; Xie, N. H.; Yu, R. H.; Stucky, G. D. Construction of $NiCo_2O_4$ nanosheets-covered $Ti_3C_2T_x$ MXene heterostructure for remarkable electromagnetic microwave absorption. *Carbon* **2022**, *193*, 26–34.

[29] Liu, J. X.; Luo, H. W.; Qian, Y.; Li, F. F.; Wu, W.; Yi, X. B.; Shi, J. Q.; Tian, Y. L.; Zhang, S. M. DDP-functionalized UiO-67

nanoparticles as lubricating oil additives for friction and wear reduction. *Tribol. Int.* **2023**, *186*, 108627.

[30] Zhou, X. F.; Jia, Z. R.; Wu, H. J.; Wu, G. L. Oxygen vacancy-induced dielectric polarization prevails in the electromagnetic wave-absorbing mechanism for Mn-based MOFs-derived composites. *Adv. Funct. Mater.* **2022**, *32*, 2204499.

[31] Li, Z. H.; Feng, L.; Huo, G. H.; Hao, J. Y.; Li, C.; He, Z. Z.; Sheremet, E.; Xu, Y. D.; Liu, J. X. Self-assembly of nanoporous ZIF-8-based superstructures for robust chemical sensing of solvent vapors. *ACS Appl. Nano Mater.* **2024**, *7*, 3479–3487.

[32] Jiang, M.; Cao, X. P.; Zhu, D. D.; Duan, Y. X.; Zhang, J. M. Hierarchically porous N-doped carbon derived from ZIF-8 nanocomposites for electrochemical applications. *Electrochim. Acta* **2016**, *196*, 699–707.

[33] Song, D. D.; Jiang, X. Y.; Li, Y. S.; Lu, X.; Luan, S. R.; Wang, Y. Z.; Li, Y.; Gao, F. M. Metal-organic frameworks-derived MnO_2/Mn_3O_4 microcuboids with hierarchically ordered nanosheets and Ti_3C_2 MXene/Au NPs composites for electrochemical pesticide detection. *J. Hazard. Mater.* **2019**, *373*, 367–376.

[34] Ren, Y. Y.; Yang, L.; Wang, L. D.; Xu, T. T.; Wu, G. L.; Wu, H. J. Facile synthesis, photoluminescence properties and microwave absorption enhancement of porous and hollow ZnO spheres. *Powder Technol.* **2015**, *281*, 20–27.

[35] Feng, W.; Wang, Y. M.; Chen, J. C.; Wang, L.; Guo, L. X.; Ouyang, J. H.; Jia, D. C.; Zhou, Y. Reduced graphene oxide decorated with *in-situ* growing ZnO nanocrystals: Facile synthesis and enhanced microwave absorption properties. *Carbon* **2016**, *108*, 52–60.

[36] Feng, Y.; Lu, H. Q.; Gu, X. L.; Qiu, J. H.; Jia, M. M.; Huang, C. B.; Yao, J. F. ZIF-8 derived porous N-doped ZnO with enhanced visible light-driven photocatalytic activity. *J. Phys. Chem. Solids* **2017**, *102*, 110–114.

[37] Yang, X. B.; Wen, Z. D.; Wu, Z. L.; Luo, X. T. Synthesis of ZnO/ZIF-8 hybrid photocatalysts derived from ZIF-8 with enhanced photocatalytic activity. *Inorg. Chem. Front.* **2018**, *5*, 687–693.

[38] Seo, Y. K.; Kumar, S.; Kim, G. H. Analysis of assembling ZnO nanoparticles into nanogap electrodes for nanoscale electronic device applications. *J. Nanosci. Nanotechnol.* **2011**, *11*, 4852–4862.

[39] Zhou, R.; Ma, M. W.; Zhu, R. Q.; Miao, P.; Liu, P.; Kong, J. ZnO/nitrogen-doped carbon nanocomplex with controlled morphology for highly efficient electromagnetic wave absorption. *J. Mater. Sci. Technol.* **2022**, *114*, 206–214.

[40] Bhat, A.; Anwer, S.; Bhat, K. S.; Mohideen, M. I. H.; Liao, K.; Qurashi, A. Prospects challenges and stability of 2D MXenes for clean energy conversion and storage applications. *npj 2D Mater. Appl.* **2021**, *5*, 61.

[41] K.; Yin, X. W.; Wu, H.; Hou, Z. X.; Song, C. Q.; Li, X. L.; Zhang, L. T.; Cheng, L. F. Ti_3C_2 MXenes with modified surface for high-performance electromagnetic absorption and shielding in the X-band. *ACS Appl. Mater. Interfaces* **2016**, *8*, 21011–21019.

[42] Zhao, B.; Zhang, X.; Deng, J. S.; Bai, Z. Y.; Liang, L. Y.; Li, Y.; Zhang, R. A novel sponge-like 2D Ni/derivative heterostructure to strengthen microwave absorption performance. *Phys. Chem. Chem. Phys.* **2018**, *20*, 28623–28633.

[43] Zhi, D. D.; Li, T.; Li, J. Z.; Ren, H. S.; Meng, F. B. A review of three-dimensional graphene-based aerogels: Synthesis, structure and application for microwave absorption. *Composites Part B: Eng.* **2021**, *211*, 108642.

[44] Chang, Q.; Liang, H. S.; Shi, B.; Wu, H. J. Microstructure induced dielectric loss in lightweight Fe_3O_4 foam for electromagnetic wave absorption. *iScience* **2022**, *25*, 103925.

[45] C.; Wang, Q. Y.; Zhou, X. D.; Kara, U. I.; Mamtani, R. S.; Lv, H. L.; Zhang, M.; Yang, Z. H.; Li, Y. J.; Wang, C. X. et al. An angle-insensitive electromagnetic absorber enabling a wideband absorption. *J. Mater. Sci. Technol.* **2022**, *113*, 33–39.

[46] Zhang, X. F.; Rao, Y.; Guo, J. J.; Qin, G. W. Multiple-phase carbon-coated $FeSn_2$/Sn nanocomposites for high-frequency microwave absorption. *Carbon* **2016**, *96*, 972–979.

[47] Han, X. P.; Huang, Y.; Ding, L.; Song, Y.; Li, T. H.; Liu, P. B. $Ti_3C_2T_x$ MXene nanosheet/metal-organic framework composites for microwave absorption. *ACS Appl. Nano Mater.* **2021**, *4*, 691–701.